Experimental demonstration of a nanobeam Fano laser

Dong, Gaoneng; Xiong, Meng; Dimopoulos, Evangelos; Sakanas, Aurimas; Semenova, Elizaveta; Yvind, Kresten; Yu, Yi; Mørk, Jesper

Published in:
Optics Express

Link to article, DOI:
10.1364/OE.511425

Publication date:
2024

Document Version
Publisher's PDF, also known as Version of record

Research Article Vol. 32, No. 4 / 12 Feb 2024 / Optics Express 5242
Optics EXPRESS

Experimental demonstration of a nanobeam Fano laser

GAONENG DONG,[1,2] MENG XIONG,[1,2] EVANGELOS DIMOPOULOS,[1,2] AURIMAS SAKANAS,[1] ELIZAVETA SEMENOVA,[1,2] KRESTEN YVIND,[1,2] YI YU,[1,2,3] AND JESPER MØRK[1,2,*]

[1]DTU Electro, Technical University of Denmark, 2800 Kgs. Lyngby, Denmark
[2]NanoPhoton - Center for Nanophotonics, Technical University of Denmark, 2800 Kgs. Lyngby, Denmark
[3]yiyu@dtu.dk
[*]jesm@dtu.dk

Abstract: Microscopic single-mode lasers with low power consumption, large modulation bandwidth, and ultra-narrow linewidth are essential for numerous applications, such as on-chip photonic networks. A recently demonstrated microlaser using an optical Fano resonance between a discrete mode and a continuum of modes to form one of the mirrors, i.e., the so-called Fano laser, holds great promise for meeting these requirements. Here, we suggest and experimentally demonstrate what we believe is a new configuration of the Fano laser based on a nanobeam geometry. Compared to the conventional two-dimensional photonic crystal geometry, the nanobeam structure makes it easier to engineer the phase-matching condition that facilitates the realization of a bound-state-in-the-continuum (BIC). We investigate the laser threshold in two scenarios based on the new nanobeam geometry. In the first, classical case, the gain is spatially located in the part of the cavity that supports a continuum of modes. In the second case, instead, the gain is located in the region that supports a discrete mode. We find that the laser threshold for the second case can be significantly reduced compared to the conventional Fano laser. These results pave the way for the practical realization of high-performance microlasers.

1. Introduction

On-chip optical interconnects [1] have received widespread attention since they are expected to overcome the limitations of conventional electrical interconnects [2] in terms of bandwidth and energy consumption. As a fundamental building block of on-chip optical networks, a high-performance microscopic laser with ultra-low power consumption is required. So far, several types of microscopic lasers have been demonstrated, such as photonic crystal lasers [3–10], and plasmonic lasers [11–14]. In particular, by engineering the doping and active regions of a photonic crystal laser, a microlaser with a threshold current below one microampere was demonstrated recently [10]. However, these microscopic lasers, employing conventional photonic crystal cavity designs usually have a linewidth exceeding 100 MHz [15], and the modulation bandwidth is limited by the relaxation oscillation frequency, as for macroscopic lasers.

Recently, a so-called Fano laser, which employs an optical Fano resonance to realize one of the mirrors, was demonstrated [16,17], showing the ability to overcome these limitations. Using a passive side-coupled nanocavity in the Fano laser, a microscopic laser with a record linewidth of 5.8 MHz was achieved [18]. The Fano laser was also theoretically predicted to enable THz-modulation bandwidth by tuning the resonance of the side-coupled nanocavity [16,19]. The Fano laser shows rich behavior due to the unique properties of the narrowband Fano mirror, including single-mode lasing [17], self-pulsing [17,20], cavity dumping [21], Q-switching [22], and suppression of the feedback-induced instabilities of lasers [23]. It was also shown that

#511425 https://doi.org/10.1364/OE.511425
Journal © 2024 Received 10 Nov 2023; revised 16 Jan 2024; accepted 16 Jan 2024; published 30 Jan 2024

Optics EXPRESS

the Fano laser could implement the nonlinear activation function required for neuromorphic photonic computing [22]. In all these schemes, the Fano laser demonstrations were based on a two-dimensional photonic crystal platform, suffering from several limitations. Firstly, to satisfy the laser oscillation condition, the length of the laser cavity (L-cavity), i.e., the region between the Fano mirror and a conventional bandgap mirror, needs to be adjusted with a precision of a few nanometers [24], which is difficult due to the discrete nature of two-dimensional photonic crystals. Thus, individual air holes are modified, i.e., geometrically altered or completely "removed" in a localized region in order to create a Fabry-Pérot BIC, and the L-cavity length cannot be continuously tuned over a large range. Secondly, the slow-light effect in the line-defect waveguide may lead to band-edge lasing [25–27]. Lastly, the coupling of the photonic crystal waveguide to an ordinary strip waveguide, used e.g. for silicon circuitry, will impose a relatively large loss and reflection [28]. Furthermore, in previous works [17,18,21], the laser gain was spatially located in the L-cavity; we shall show that this classical Fano laser configuration is not always the optimum case.

In this work, we demonstrate a new Fano laser geometry based on a photonic crystal nanobeam cavity, which can overcome the limitations of previous Fano lasers based on the two-dimensional photonic crystal platform. By adopting this scheme, we experimentally investigate the threshold of a new configuration of the Fano laser in which the gain is situated in the side-coupled nanocavity used to form the Fano resonance, rather than the L-cavity, as conventionally done. By studying the threshold dependence on the cavity length of the Fano laser, we find that the minimum threshold of the new configuration of the Fano laser approaches that of an isolated nanocavity laser, which is typically lower than the minimum threshold obtained in the classical configuration of the Fano laser. It is also an important feature of the demonstrated geometry that it allows evanescent coupling to a silicon waveguide [6], as an alternative to monolithically integrated silicon light sources [29].

2. Concept, design, and fabrication

2.1. Concept and design

The classical configuration of a Fano laser (Fig. 1(a)) consists of a broadband left mirror, a waveguide, and a narrowband right (Fano) mirror, realized by side-coupling a nanocavity to the waveguide. Conventionally, the gain of the Fano laser is located in the region (denoted the L-cavity) between the two mirrors. Here, we consider a new configuration (Fig. 1(b)) where the gain is instead located in the side-coupled nanocavity. In this work, since the entire device contains layers of quantum dots (QDs) in the middle of the membrane, the same as in our previous work [17], the spatial location of the gain is determined by the region excited by the pump beam.

Figure 1(c) shows the schematic of a Fano laser based on a photonic crystal nanobeam cavity. The broadband left mirror is formed by simply terminating the waveguide with holes, while the narrowband right mirror originates from a Fano interference between the continuum of modes of the strip waveguide and a discrete mode of the nanobeam cavity. At steady state, the oscillating mode of the Fano laser fulfills the oscillation condition, valid for both configurations,

$$r_L r_R \exp(2ikL) = 1 \tag{1}$$

where r_L and r_R are the field reflection coefficients of the left and right mirrors, respectively, k is the wavenumber of the strip waveguide with an effective cavity length of L. By considering the absolute value and the argument of Eq. (1), it is separated into equations for the threshold gain and the phase of the possible oscillating modes (Supplement A). Due to the strong frequency dependence of the Fano mirror reflectivity and phase, the two equations are strongly coupled. Thus, the gain and phase conditions are only fulfilled simultaneously for specific lengths of the L-cavity.

Optics EXPRESS

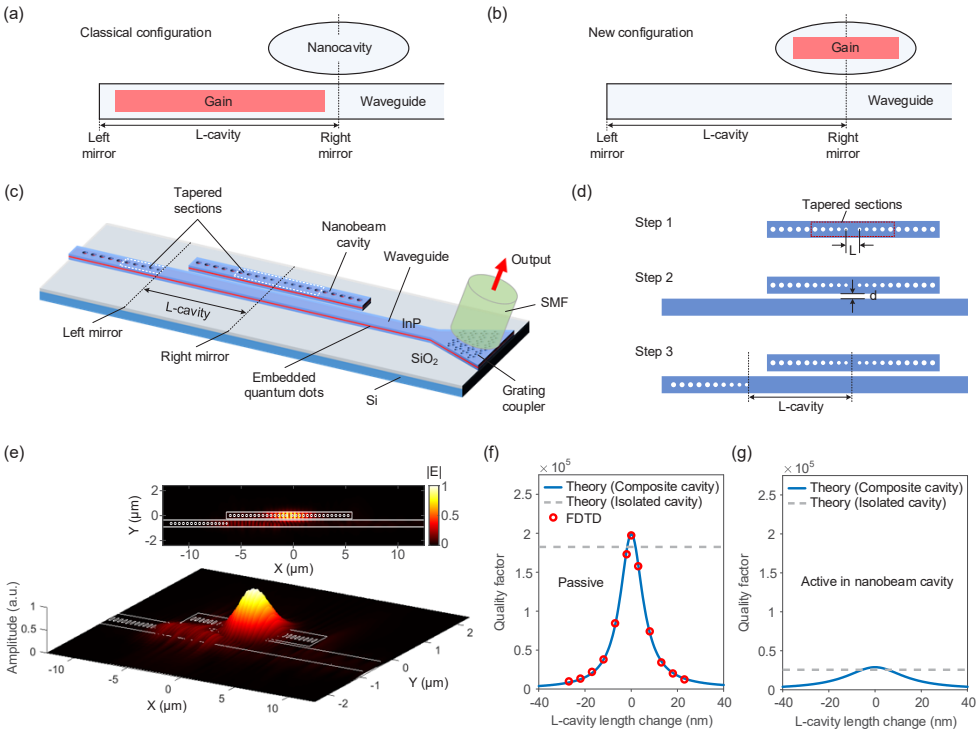

Fig. 1. Nanobeam Fano laser. (a) – (b) Classical (a) and new (b) configurations of Fano laser in which the gain is located in the L-cavity and the side-coupled nanocavity, respectively. (c) Schematic of device geometry. A single-mode fiber (SMF) is used to extract the output light through the grating coupler. (d) Illustration of the design process of the nanobeam Fano laser. (e) Calculated electric field profile (|E|) of the Fano mode in the central plane of the InP layer when the lasing wavelength coincides with the peak reflectivity of the Fano mirror. Inset: top view of the electrical field profile. (f) FDTD-simulated (red circles) and calculated (blue line) quality factors of the passive composite cavity versus change of the L-cavity length from the reference cavity length, for which the oscillating frequency coincides with the reflectivity peak of the Fano mirror. The gray dashed line shows the corresponding quality factor of the isolated nanobeam cavity. (g) Calculated quality factors of the composite cavity and the isolated nanobeam cavity with active material in the nanobeam cavity. In (f) and (g), the intrinsic quality factor Q_v of the nanobeam cavity is 1.8×10^5, while the coupling quality factor Q_c between the nanobeam cavity and the waveguide is 900. The absorption quality factor Q_a of the nanobeam cavity due to active material is 2.7×10^4 in (g).

The design process of the nanobeam Fano laser can be divided into the following three steps (Fig. 1(d)): firstly, by adding tapered sections to the center of the nanobeam cavity to reduce the mode mismatch [30], a nanobeam cavity with a high intrinsic quality factor is achieved [31–33]; then, the coupling strength between the optimized nanobeam cavity and the side-coupled waveguide is tuned to get a low loaded quality factor, so that wavelengths close to the resonance of the discrete cavity mode are reflected with near-unity reflectivity; finally, by precisely adjusting the cavity length, i.e., the distance between the (effective) positions of the left and right mirrors, a composite cavity with a peak quality factor of 1.97×10^5 is achieved at a cavity length of 5.957 μm (Fig. 1(f)), meaning that the wavelength of the oscillating mode coincides with the reflectivity peak of the Fano mirror. The quality factors simulated using a finite-difference time-domain (FDTD) method agree well with the theoretical results for a passive composite cavity [34]. When

Optics EXPRESS

the inevitable propagation loss [35] induced by the active material in the nanobeam cavity is taken into account, the corresponding quality factor of the composite cavity decreases, as shown in Fig. 1(g). Similar to the Fano laser based on two-dimensional photonic crystals, the field (calculated by *Lumerical FDTD* [36]) is mainly localized in the side-coupled nanobeam cavity (Fig. 1(e)). In order to couple the laser light to a fiber, a grating coupler is included at the end of the waveguide. The grating coupler is designed using the approach described in Ref. [37,38]. Compared to suspended membrane structures used in earlier works [17,18,21], the present nanobeam geometry is bonded to a silicon substrate with a silica layer (Fig. 1(c)), providing much better mechanical stability and heat dissipation [39].

2.2. Fabrication

The samples are fabricated on a heterogeneous integrated InP-on-Si wafer, following the fabrication process shown in Fig. 2(a). First of all, the InP wafer, which has a 250-nm-thick InP membrane containing three layers (8 nm/layer) of InAs QDs separated by a 30-nm InP spacer, is directly bonded to the Si substrate with 1.1-μm thermal oxide. Then, the InP substrate is removed by chemical etching in HCl terminating at an InGaAs etch-stop layer, which is later wet etched away in the H_2SO_4:H_2O_2:H_2O mixture. The device structure is patterned on a photoresist (CSAR) through e-beam exposure and then transferred to a SiN_x hard mask and finally to the InP membrane through a two-step inductively coupled plasma (ICP) etching. A thin layer of

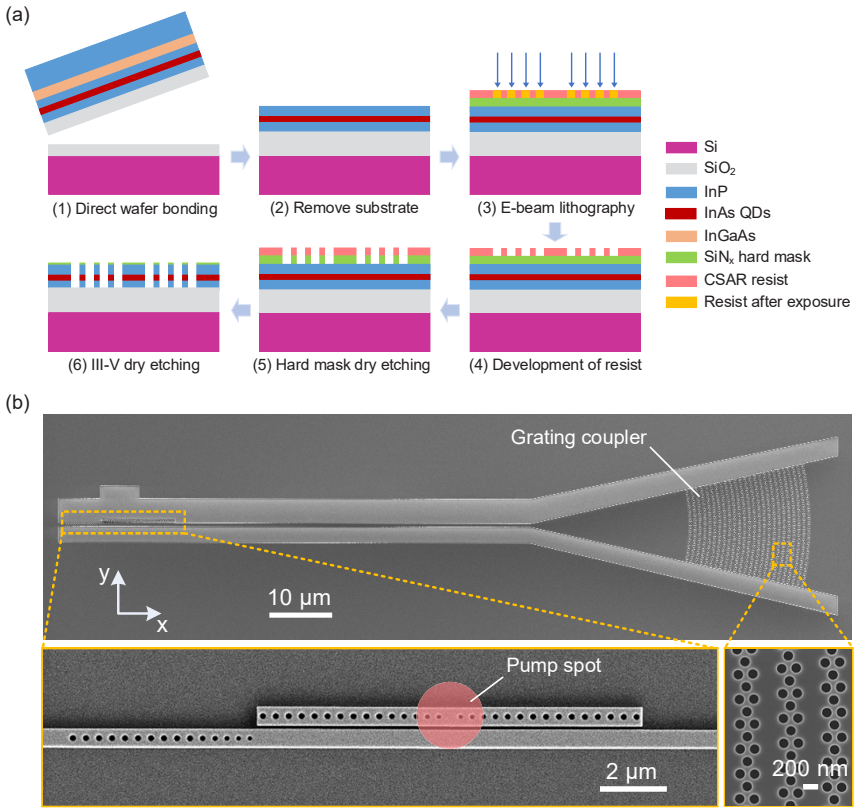

Fig. 2. Fabrication process. (a) Fabrication steps of the nanobeam Fano laser. (b) Scanning electron microscopy (SEM) images of a fabricated nanobeam Fano laser. The insets are enlarged images of the Fano laser (left) and the grating coupler (right). The red circle shows the region where the laser is optically pumped.

Optics EXPRESS

the residual SiN_x (~20 nm) is left on the top of the InP membrane. The simulated results show that the residual SiN_x hard mask will not degrade the quality factor of the composite cavity with a proper L-cavity length. The fully etched grating coupler is fabricated simultaneously with the nanobeam Fano laser. Scanning electron microscopy (SEM) images of a fabricated device are shown in Fig. 2(b). The device has a small footprint of $1.26 \times 17\ \mu m^2$ (see the left inset in Fig. 2(b)). Even though the QDs are distributed across the entire device, the measured total propagation loss of the waveguide and the grating coupler is as low as −6.7 dB at the lasing wavelength due to their relatively short lengths (Supplement C).

3. Results

3.1. Lasing characteristics and mode pattern

The sample is vertically pumped with a 980-nm continuous-wave laser diode using a micro-photoluminescence setup, and the laser output is extracted via the grating coupler with a single-mode fiber (Supplement B). The pump position and area are precisely controlled under the monitoring of an infrared camera. The pump area mainly covers the nanobeam cavity, as illustrated by the red-shaded area in Fig. 2(b), meaning that the gain is provided by the nanobeam cavity. During the measurements, a 20× objective (the numerical aperture, NA, is 0.4) with a long working distance of 25 mm is used to provide sufficient space to insert the fiber couplers between the sample and the objective.

The laser output power, collected by the fiber, versus pump power is depicted in Fig. 3(a) and shows a clear transition to lasing at a threshold pump power of 8.3 dBm. The measured data are well-fitted by a conventional rate equation model [35], leading to an estimated spontaneous emission β-factor of 0.23%. The optical spectrum (Fig. 3(b)) shows a single mode at 1551 nm with contrast as high as 40 dB and a peak power of −40 dBm in the fiber, i.e., a peak power of −33.7 dBm in the output waveguide. Figure 3(c) depicts the center wavelength and full width at half maximum (FWHM) of the central peak as a function of pump power. In the spontaneous emission regime, the wavelength gradually blue-shifts with pump power due to the carrier-filling effect. Above the threshold, the lasing wavelength red-shifts due to heating, which is mainly induced by the high optical power density of the pump light. The laser linewidth, obtained as the FWHM of the spectral peak, decreases with the pump power and saturates close to the threshold, where the resolution (0.02 nm) of the optical spectrum analyzer is reached.

To confirm that lasing in the Fano laser is facilitated by the composite cavity formed by the L-cavity and the side-coupled nanobeam cavity rather than just the nanobeam cavity, we fabricated and measured a similar device but without the broadband mirror in the strip waveguide, as shown in the inset of Fig. 3(e). In this case, we only observe a weak spontaneous emission peak from the device, although the pump power and the pump position are the same as for the Fano laser investigated above. This is in agreement with the very low quality factor (~ 900) of the nanobeam cavity coupled to an open waveguide. In contrast, the composite quality factor of the Fano laser is as high as 1.3×10^4 at the reflectivity peak of the Fano mirror (Fig. 4(b)), leading to a much lower threshold power.

Next, the infrared image of the lasing pattern of a Fano laser is measured with a 50× objective (NA = 0.65), as seen in the upper panel of Fig. 3(d). When the oscillation condition is fulfilled, the laser field pattern is distributed over the L-cavity and the nanobeam cavity, with the latter being especially bright. This is in good agreement with the calculated field intensity distribution on the top surface of the device, shown in the lower panel of Fig. 3(d).

3.2. Threshold characteristics

An important advantage of the nanobeam Fano laser is that the length of the L-cavity can be changed in a continuous manner, as opposed to the case of a line-defect waveguide in a

Optics EXPRESS

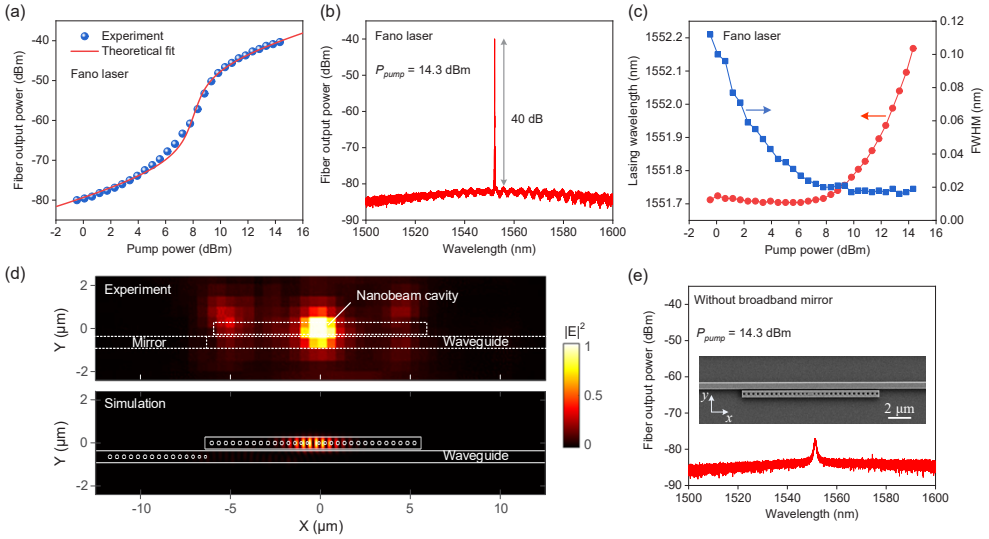

Fig. 3. Lasing characteristics of nanobeam Fano laser. (a) Measured fiber output power versus pump power. (b) Measured optical spectrum for a pump power of 14.3 dBm. (c) Measured emission wavelength (red) and full width at half maximum (FWHM, blue) versus pump power. (d) Measured (normalized, upper panel) infrared image of the lasing pattern of a fabricated Fano laser and simulated (normalized, lower panel) electric field intensity distribution ($|E|^2$) on the top surface of the Fano structure when the oscillating wavelength coincides with the reflectivity peak of the Fano mirror. (e) The measured optical spectrum of a nanobeam cavity coupled to a waveguide (the inset is the SEM image) for a pump power of 14.3 dBm. In (a) – (c) and (e), the pump power was measured after the objective (NA=0.4, 20 ×), and the resolution of the optical spectrum analyzer was 0.02 nm.

two-dimensional photonic crystal platform. This means that the phase oscillation condition can be continuously tuned, and the nanobeam Fano laser is ideally suited to investigate the threshold dependence on the cavity length. This dependence is an important characteristic of Fano lasers [24] and is closely related to the properties of a bound-state-in-the-continuum [18].

During the threshold characterization, the lasing light is collected from the top of the nanobeam cavity with a 50× objective. Figure 4(a) shows the measured threshold power versus the L-cavity length. The length is measured relative to the reference cavity length, where the lasing wavelength coincides with the reflectivity peak of the Fano mirror. We measured three sets of Fano lasers. The radius of the holes did not vary within the same set but differed within a few nanometers among different sets, which, according to simulations, will not significantly affect the intrinsic quality factor of the nanobeam cavity. The measurement results clearly show that the threshold power gradually increases when the L-cavity length is detuned from the optimum reference cavity length, in good agreement with the theoretical prediction (Supplement 1). The dependence of the threshold power is nearly symmetric with respect to L-cavity length due to the low linewidth enhancement factor α, which is estimated to be 0.2 by fitting the measured data. The α-factor is relatively low because of the use of QDs [40,41] as active material in the Fano laser, which agrees with the very small blue shift (0.02 nm) of the emission wavelength when the Fano laser operates in the spontaneous emission regime (Fig. 3(c)). Although the un-pumped active material in the L-cavity induces propagation loss [35], the calculated results show that this loss just slightly increases the threshold power. This is in correspondence with the quality factors of the different modes of the composite cavity (Fig. 4(b)). Despite the sensitive nature of the bound-state-in-the continuum, requiring the fulfillment of the standing wave condition for the mode at the resonance

Optics EXPRESS

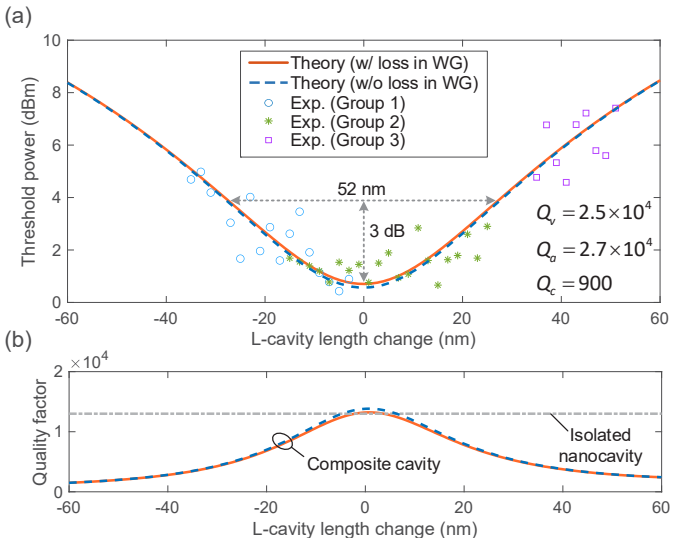

Fig. 4. Threshold characteristics of nanobeam Fano laser. (a) Measured (marks) and theoretical (lines) threshold power versus cavity length change of Fano laser. The cavity length change refers to the length variation with respect to a reference cavity length where the lasing wavelength coincides with the reflectivity peak of the Fano mirror. The red solid and blue dashed curves are the calculated results with and without a propagation loss (α_i = 5cm^{-1}) due to active material in the waveguide (WG), respectively. The calculated intrinsic (Q_v), absorption (Q_a), and coupling (Q_c) quality factors of the nanocavity making the Fano mirror are 2.5×10^4, 2.7×10^4, and 900, respectively. The measured threshold power refers to the value after the objective (NA =0.65, 50 ×). (b) Calculated corresponding quality factors of the composite cavity in (a). As a reference, the horizontal gray dashed line indicates the total quality factor of the corresponding isolated nanocavity.

of the nanocavity, the 3-dB bandwidth of the threshold power, defined as twice the length change ($2\Delta L$) of the L-cavity required to double the threshold power, is as large as 52 nm, which is easily achievable using modern nanofabrication technologies. This relatively large 3-dB bandwidth is attributed to the highly dispersive Fano mirror [24] because a large phase change can be achieved in the Fano mirror by only slightly changing the oscillation frequency to compensate for the phase change caused by the L-cavity length variation. The measured minimum threshold power (~0.6 dBm), depicted in Fig. 4(a), is significantly lower than the threshold value (8.3 dBm) deduced earlier from the lasing characteristic measurements (see Fig. 3(a) in section 3.1). This is due to the larger magnification and NA of the objective used for the measurements reported in Fig. 4, which leads to a higher pumping efficiency due to a smaller diameter (2 μm) of the pump spot.

3.3. *Threshold comparisons*

Finally, we compared the threshold power of the new configuration of the Fano laser with several conventional structures, including the isolated nanobeam laser, the classical configuration of the Fano laser, and the waveguide-coupled nanobeam cavity (Fig. 5). In all cases, the emitted light was collected from the top of the nanobeam cavity with a 50× objective. Figure 5(a) shows the collected output peak power versus pump power of the new Fano laser configuration for the situation where the laser wavelength coincides with the reflectivity peak of the Fano mirror, i.e., the device with the minimum threshold power in Fig. 4(a). The minimum threshold power of the new Fano laser configuration (0.9 ± 0.3 dBm) is very close to the value of the isolated nanobeam lasers (−0.4 ± 0.3 dBm) (Fig. 5(a)), which agrees well with our theory (Supplement 1). The

Optics EXPRESS

slightly higher measured value for the Fano laser is mainly due to the reflectivity of the left mirror being lower than unity and the propagation loss in the L-cavity. Figures 5(b) and 5(c) show the lasing spectra of the new Fano laser configuration and the isolated nanobeam lasers at a pump power of 8.43 dBm. Compared to the isolated nanobeam laser, the Fano laser also provides an effective means of achieving in-plane output coupling (Fig. 3), in addition to collecting the laser light from the top of the nanobeam cavity. When the pump spot was moved to the L-cavity, and the pump power was kept fixed (Fig. 5(d)), the devices working in the classical configuration did not lase but rather showed spontaneous emission peaks. This is due to the higher threshold power of the classical configuration. The waveguide-coupled structure did not lase either (Fig. 5(e)), in good agreement with our theory (Supplement 1).

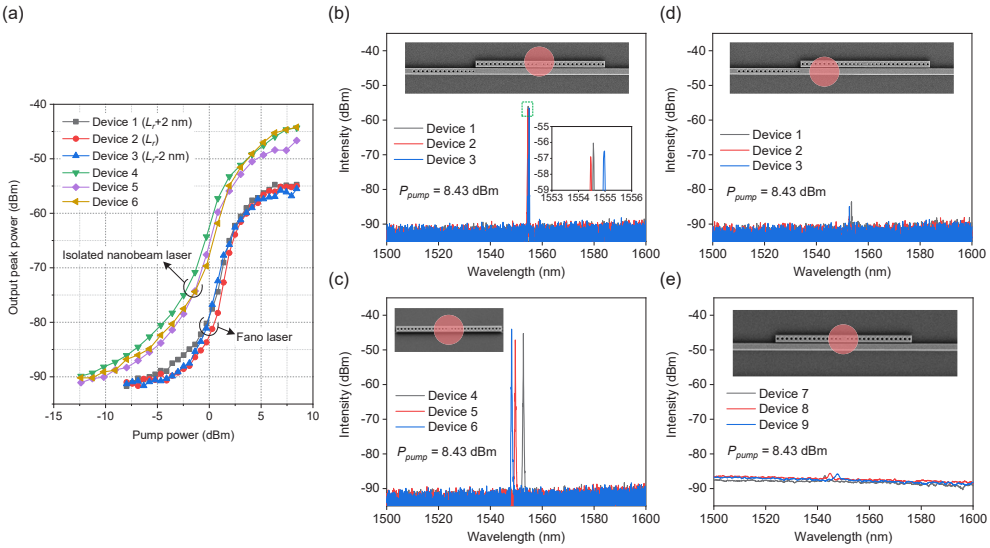

Fig. 5. Comparison of laser threshold for different cavity geometries. (a) Collected output peak power of the lasing spectra versus pump power of the new configuration of Fano laser and the isolated nanobeam laser. L_r is the reference length of the L-cavity, for which the lasing wavelength coincides with the peak reflectivity of the Fano mirror. (b) – (e) Emission spectra for a fixed pump power of 8.43 dBm for different cavity geometries: (b) the Fano laser where the nanobeam cavity is pumped, (c) the isolated nanobeam laser, (d) the Fano laser where the L-cavity is pumped, and (e) the nanobeam cavity coupled with a waveguide. In (a) – (e), the light was collected from the top of the nanobeam cavity. The pump power was measured after the objective (NA=0.65, 50 ×). The red-shaded region represents the pump spot in (b) – (e).

4. Discussion and conclusion

In the present work, QDs are evenly distributed over the entire laser structure, implying that un-pumped regions are lossy. Since the loss of the un-pumped region is rather small, estimated at 5 cm^{-1}, the propagation loss of the waveguide and grating coupler is, however, not a dominant factor. An important future goal is to apply the buried heterostructure technology [7,10,42] to nanobeams. In that case, the laser threshold of the new configuration would be further reduced, approaching the value of the isolated nanobeam laser. An electrically driven nanobeam Fano laser is also feasible by engineering the electrodes and the nanobeam structure, such as using a vertical coupling scheme [6]. Furthermore, by incorporating a microscopic heater [43,44] to

Optics EXPRESS

independently tune the laser phase, one can ensure that the minimum threshold is obtained, even in the case of fabrication imperfections.

In conclusion, we have experimentally demonstrated a new geometry of a Fano laser based on an InP-on-silicon nanobeam cavity, showing continuous-wave single-mode lasing at room temperature. The nanobeam Fano laser overcomes the limitations of previously demonstrated Fano lasers based on the two-dimensional photonic crystal platform. By investigating the threshold power dependence on the cavity length of the Fano laser, we found that the threshold power varies by less than a factor of two from its minimum value within a length tuning range of 52 nm. Moreover, we characterized the laser thresholds for different pumping configurations. We find that the minimum threshold power of the new Fano laser configuration, where the optical gain is provided by the nanocavity rather than the conventional laser cavity, can approach that of the isolated nanobeam laser counterpart. The new Fano laser provides an effective means to achieve in-plane output coupling and offers the possibilities for pulse generation [17] and linewidth reduction [18], as shown earlier. Also, the nanobeam Fano laser facilitates chip-scale optoelectronic integration, e.g., by including vertical and hybrid techniques [6], with the potential to realize low-energy, high-speed optical communication and computation [45].

Funding. Villum Fonden via the Young Investigator Program (42026) and via the NATEC Center (8692 NATEC II); Danmarks Grundforskningsfond (DNRF147 NanoPhoton); European Research Council (834410 FANO).

Disclosures. The authors declare no competing interests.

Data availability. Data underlying the results presented in this paper may be obtained from the authors upon reasonable request.

Supplemental document. See Supplement 1 for supporting content.

References

1. D. Miller, "Device Requirements for Optical Interconnects to Silicon Chips," Proc. IEEE **97**(7), 1166–1185 (2009).
2. I. L. Markov, "Limits on fundamental limits to computation," Nature **512**(7513), 147–154 (2014).
3. O. Painter, R. K. Lee, A. Scherer, *et al.*, "Two-Dimensional Photonic Band-Gap Defect Mode Laser," Science **284**(5421), 1819–1821 (1999).
4. H.-G. Park, S.-H. Kim, S.-H. Kwon, *et al.*, "Electrically Driven Single-Cell Photonic Crystal Laser," Science **305**(5689), 1444–1447 (2004).
5. B. Ellis, M. A. Mayer, G. Shambat, *et al.*, "Ultralow-threshold electrically pumped quantum-dot photonic-crystal nanocavity laser," Nat. Photonics **5**(5), 297–300 (2011).
6. G. Crosnier, D. Sanchez, S. Bouchoule, *et al.*, "Hybrid indium phosphide-on-silicon nanolaser diode," Nat. Photonics **11**(5), 297–300 (2017).
7. K. Takeda, T. Sato, A. Shinya, *et al.*, "Few-fJ/bit data transmissions using directly modulated lambda-scale embedded active region photonic-crystal lasers," Nat. Photonics **7**(7), 569–575 (2013).
8. K.-Y. Jeong, Y.-S. No, Y. Hwang, *et al.*, "Electrically driven nanobeam laser," Nat. Commun. **4**(1), 2822 (2013).
9. E. Dimopoulos, A. Sakanas, A. Marchevsky, *et al.*, "Electrically-Driven Photonic Crystal Lasers with Ultra-low Threshold," Laser Photonics Rev. **16**(11), 2200109 (2022).
10. E. Dimopoulos, M. Xiong, A. Sakanas, *et al.*, "Experimental demonstration of a nanolaser with a sub-μA threshold current," Optica **10**(8), 973 (2023).
11. M. Khajavikhan, A. Simic, M. Katz, *et al.*, "Thresholdless nanoscale coaxial lasers," Nature **482**(7384), 204–207 (2012).
12. R. F. Oulton, V. J. Sorger, T. Zentgraf, *et al.*, "Plasmon lasers at deep subwavelength scale," Nature **461**(7264), 629–632 (2009).
13. M. T. Hill, M. Marell, E. S. P. Leong, *et al.*, "Lasing in metal-insulator-metal sub-wavelength plasmonic waveguides," Opt. Express **17**(13), 11107–11112 (2009).
14. M. A. Noginov, G. Zhu, A. M. Belgrave, *et al.*, "Demonstration of a spaser-based nanolaser," Nature **460**(7259), 1110–1112 (2009).
15. J. Kim, A. Shinya, K. Nozaki, *et al.*, "Narrow linewidth operation of buried-heterostructure photonic crystal nanolaser," Opt. Express **20**(11), 11643–11651 (2012).
16. J. Mork, Y. Chen, and M. Heuck, "Photonic crystal Fano laser: terahertz modulation and ultrashort pulse generation," Phys. Rev. Lett. **113**(16), 163901 (2014).
17. Y. Yu, W. Xue, E. Semenova, *et al.*, "Demonstration of a self-pulsing photonic crystal Fano laser," Nat. Photonics **11**(2), 81–84 (2017).
18. Y. Yu, A. Sakanas, A. R. Zali, *et al.*, "Ultra-coherent Fano laser based on a bound state in the continuum," Nat. Photonics **15**(10), 758–764 (2021).

Optics EXPRESS

19. A. R. Zali, M. K. Moravvej-Farshi, Y. Yu, *et al.*, "Small and Large Signal Analysis of Photonic Crystal Fano Laser," J. Lightwave Technol. **36**(23), 5611–5616 (2018).
20. T. S. Rasmussen, Y. Yu, and J. Mork, "Theory of Self-pulsing in Photonic Crystal Fano Lasers," Laser Photonics Rev. **11**(5), 1700089 (2017).
21. G. Dong, S. L. Liang, A. Sakanas, *et al.*, "Cavity dumping using a microscopic Fano laser," Optica **10**(2), 248–254 (2023).
22. T. S. Rasmussen, Y. Yu, and J. Mork, "All-optical non-linear activation function for neuromorphic photonic computing using semiconductor Fano lasers," Opt. Lett. **45**(14), 3844–3847 (2020).
23. T. S. Rasmussen, Y. Yu, and J. Mork, "Suppression of Coherence Collapse in Semiconductor Fano Lasers," Phys. Rev. Lett. **123**(23), 233904 (2019).
24. J. Mork, Y. Yu, T. S. Rasmussen, *et al.*, "Semiconductor Fano Lasers," IEEE J. Select. Topics Quantum Electron. **25**(6), 1–14 (2019).
25. K. Sakai, E. Miyai, T. Sakaguchi, *et al.*, "Lasing band-edge identification for a surface-emitting photonic crystal laser," IEEE J. Select. Areas Commun. **23**(7), 1335–1340 (2005).
26. C.-O. Cho, J. Jeong, J. Lee, *et al.*, "Photonic crystal band edge laser array with a holographically generated square-lattice pattern," Appl. Phys. Lett. **87**(16), 161102 (2005).
27. H.-Y. Ryu, S.-H. Kwon, Y.-J. Lee, *et al.*, "Very-low-threshold photonic band-edge lasers from free-standing triangular photonic crystal slabs," Appl. Phys. Lett. **80**(19), 3476–3478 (2002).
28. T. J. Karle, D. H. Brown, R. Wilson, *et al.*, "Planar photonic crystal coupled cavity waveguides," IEEE J. Select. Topics Quantum Electron. **8**(4), 909–918 (2002).
29. K. Xu, "Silicon electro-optic micro-modulator fabricated in standard CMOS technology as components for all silicon monolithic integrated optoelectronic systems," J. Micromech. Microeng. **31**(5), 054001 (2021).
30. C. Sauvan, G. Lecamp, P. Lalanne, *et al.*, "Modal-reflectivity enhancement by geometry tuning in Photonic Crystal microcavities," Opt. Express **13**(1), 245–255 (2005).
31. P. B. Deotare, M. W. McCutcheon, I. W. Frank, *et al.*, "High quality factor photonic crystal nanobeam cavities," Appl. Phys. Lett. **94**(12), 121106 (2009).
32. A. R. M. Zain, N. P. Johnson, M. Sorel, *et al.*, "Ultra high quality factor one dimensional photonic crystal/photonic wire micro-cavities in silicon-on-insulator (SOI)," Opt. Express **16**(16), 12084–12089 (2008).
33. P. Velha, E. Picard, T. Charvolin, *et al.*, "Ultra-High Q/V Fabry-Perot microcavity on SOI substrate," Opt. Express **15**(24), 16090–16096 (2007).
34. Y. Yu, A. R. Zali, and J. Mørk, "Theory of linewidth narrowing in Fano lasers," Phys. Rev. Research **4**(4), 043194 (2022).
35. L. A. Coldren, S. W. Corzine, and M. L. Mashanovitch, *Diode lasers and photonic integrated circuits* (John Wiley & Sons, 2012), App. 5.
36. https://www.ansys.com/products/optics/fdtd.
37. K. Yvind and J. M. Hvam, "High-efficiency, large-bandwidth silicon-on-insulator grating coupler based on a fully-etched photonic crystal structure," Appl. Phys. Lett. **96**(5), 051126 (2010).
38. F. Van Laere, T. Claes, J. Schrauwen, *et al.*, "Compact Focusing Grating Couplers for Silicon-on-Insulator Integrated Circuits," IEEE Photonics Technol. Lett. **19**(23), 1919–1921 (2007).
39. A. Bazin, P. Monnier, X. Lafosse, *et al.*, "Thermal management in hybrid InP/silicon photonic crystal nanobeam laser," Opt. Express **22**(9), 10570–10578 (2014).
40. T. C. Newell, D. J. Bossert, A. Stintz, *et al.*, "Gain and linewidth enhancement factor in InAs quantum-dot laser diodes," IEEE Photonics Technol. Lett. **11**(12), 1527–1529 (1999).
41. J. C. Norman, R. P. Mirin, and J. E. Bowers, "Quantum dot lasers—History and future prospects," J. Vac. Sci. Technol. A **39**(2), 020802 (2021).
42. S. Matsuo, A. Shinya, T. Kakitsuka, *et al.*, "High-speed ultracompact buried heterostructure photonic-crystal laser with 13 fJ of energy consumed per bit transmitted," Nat. Photonics **4**(9), 648–654 (2010).
43. Y. Zhang, Y. He, Q. Zhu, *et al.*, "Single-resonance silicon nanobeam filter with an ultra-high thermo-optic tuning efficiency over a wide continuous tuning range," Opt. Lett. **43**(18), 4518–4521 (2018).
44. H. Zhou, C. Qiu, X. Jiang, *et al.*, "Compact, submilliwatt, 2 × 2 silicon thermo-optic switch based on photonic crystal nanobeam cavities," Photon. Res. **5**(2), 108–112 (2017).
45. D. Dai, A. Fang, and J. E. Bowers, "Hybrid silicon lasers for optical interconnects," New J. Phys. **11**(12), 125016 (2009).